Monthly Notices of the ROYAL ASTRONOMICAL SOCIETY

MNRAS **501,** 4748–4758 (2021) doi:10.1093/mnras/staa3408
Advance Access publication 2020 November 4

A tale of two sites – II. Inferring the properties of minihalo-hosted galaxies with upcoming 21-cm interferometers

Yuxiang Qin [1]★ Andrei Mesinger [1] Bradley Greig[2,3] and Jaehong Park [1,4]

[1]*Scuola Normale Superiore, Piazza dei Cavalieri 7, I-56126 Pisa, Italy*
[2]*School of Physics, University of Melbourne, Parkville, VIC 3010, Australia*
[3]*ARC Centre of Excellence for All Sky Astrophysics in 3 Dimensions (ASTRO 3D), University of Melbourne, VIC 3010, Australia*
[4]*School of Physics, Korea Institute for Advanced Study (KIAS), 85 Hoegiro, Dongdaemun-gu, Seoul 02455, Republic of Korea*

Accepted 2020 October 28. Received 2020 October 28; in original form 2020 September 24

ABSTRACT

The first generation of galaxies is expected to form in minihaloes, accreting gas through H_2 cooling, and possessing unique properties. Although unlikely to be directly detected in UV/infrared surveys, the radiation from these molecular-cooling galaxies (MCGs) could leave an imprint in the 21-cm signal from the Cosmic Dawn. Here, we quantify their detectability with upcoming radio interferometers. We generate mock 21-cm power spectra using a model for both MCGs as well as more massive, atomic-cooling galaxies, allowing both populations to have different properties and scaling relations. The galaxy parameters are chosen so as to be consistent with: (i) high-redshift UV luminosity functions; (ii) the upper limit on the neutral fraction from QSO spectra; (iii) the Thomson scattering optical depth to the CMB; and (iv) the timing of the recent putative EDGES detection. The latter implies a significant contribution of MCGs to the Cosmic Dawn, if confirmed to be cosmological. We then perform Bayesian inference on two models including and ignoring MCG contributions. Comparing their Bayesian evidences, we find a strong preference for the model including MCGs, despite the fact that it has more free parameters. This suggests that if MCGs indeed play a significant role in the Cosmic Dawn, it should be possible to infer their properties from upcoming 21-cm power spectra. Our study illustrates how these observations can discriminate among uncertain galaxy formation models with varying complexities, by maximizing the Bayesian evidence.

Key words: galaxies: high-redshift – intergalactic medium – dark ages, reionization, first stars – diffuse radiation – early Universe – cosmology: theory.

1 INTRODUCTION

The first galaxies of our Universe are expected to form out of pristine gas, cooling inside so-called minihaloes (with mass $M_h \sim 10^6$–10^8 $M_\odot$) via rotational–vibrational transitions of H_2 (e.g. Haiman, Rees & Loeb 1996, 1997; Yoshida et al. 2003, 2006). The first episodes of star formation, evolution, and feedback inside these first-generation, molecular-cooling galaxies (MCGs) can be very different from later generations that were mostly built-up out of pre-enriched material inside deeper potential wells (e.g. Haiman, Abel & Rees 2000; Tumlinson & Shull 2000; Abel, Bryan & Norman 2002; Schaerer 2002; Bromm & Larson 2004; Yoshida et al. 2006; McKee & Tan 2008; Whalen et al. 2008; Turk, Abel & O'Shea 2009; Heger & Woosley 2010; Wise et al. 2012; Kimm et al. 2017; Xu et al. 2016b). Moreover, star formation inside MCGs is expected to be transient, tapering off as a growing Lyman–Werner (LW) background starts to effectively photodissociate H_2 (e.g. Johnson, Greif & Bromm 2007; Ahn et al. 2009; Holzbauer & Furlanetto 2012; Fialkov et al. 2013; Jaacks, Finkelstein & Bromm 2018; Schauer et al. 2019).

Unfortunately, MCGs are likely too faint to observe directly using UV or infrared telescopes in the foreseeable future (e.g. O'Shea et al. 2015; Xu et al. 2016b; also see Schauer, Drory & Bromm 2020 for a feasibility estimate of a moon-based near-infrared telescope and e.g. Mesinger, Johnson & Haiman 2006; Smidt et al. 2015; Hartwig, Bromm & Loeb 2018 for possible indirect detection through supernova explosion using the *James Webb Space Telescope*). Their transient nature also makes low-redshift detection or even searching for stellar relics in the nearby Universe very challenging (Beers & Christlieb 2005; Nagao et al. 2005, 2008; Tornatore, Ferrara & Schneider 2007; Lai et al. 2008; Suda et al. 2008; Roederer et al. 2014; Liu & Bromm 2020).

A promising alternative is to study MCGs through the imprint their radiation fields leave in the intergalactic medium (IGM; Fialkov et al. 2013; Mirocha et al. 2018; Muñoz 2019). In the standard hierarchical structure formation paradigm, there should have existed a period at the start of the Cosmic Dawn in which the radiation backgrounds were dominated by MCGs. If we can observe IGM properties at a high enough redshift, we could indirectly study the properties of MCGs (e.g. Ciardi et al. 2006; McQuinn et al. 2007; Ahn et al. 2012; Mesinger, McQuinn & Spergel 2012; Visbal, Haiman & Bryan 2015; Miranda et al. 2017; Koh & Wise 2018).

Luckily, the cosmic 21-cm signal is set to revolutionize our understanding of the early Universe (for a recent review, see Mesinger 2019). Sourced by the spin-flip transition of neutral hydrogen, the

★ E-mail: Yuxiang.L.Qin@gmail.com

cosmic 21-cm signal is sensitive to the ionization and thermal state of the IGM. These are in turn determined by the ionizing, soft UV and X-ray emission from the first galaxies. Therefore, the high-redshift 21-cm signal should encode information about the birth, disappearance, spatial distribution, and typical spectral energy distributions (SEDs) of MCGs.

Many experiments are striving to measure the signal. These can be broadly divided into global signal experiments and interferometers measuring 21-cm fluctuations. The former includes the Shaped Antenna measurement of the background RAdio Spectrum (Singh et al. 2018), the Large-aperture Experiment to Detect the Dark Age (Price et al. 2018), Probing Radio Intensity at high-Z from Marion (Philip et al. 2019), and the Experiment to Detect the Global EoR (i.e. epoch of reionization) Signature (EDGES; Bowman et al. 2018). The latter has recently claimed a detection with an absorption feature at $z \sim 17$, inciting much debate as to its cosmological origin (e.g. Ewall-Wice et al. 2018; Fialkov, Barkana & Cohen 2018; Hills et al. 2018; Muñoz & Loeb 2018; Bradley et al. 2019; Mebane, Mirocha & Furlanetto 2020; Mirocha & Furlanetto 2019; Sims & Pober 2019; Qin et al. 2020). Existing interferometers, such as the Low-Frequency Array (LOFAR[1]; van Haarlem et al. 2013; Patil et al. 2017), the Murchison Widefield Array (MWA[2]; Tingay et al. 2013; Beardsley et al. 2016), and the Precision Array for Probing Epoch of Reionization (PAPER[3]; Parsons et al. 2010), are focusing on measuring the 21-cm power spectrum (PS), generally at $z < 10$. These instruments are serving as precursors and pathfinders for the next-generation radio telescopes: the Hydrogen Epoch of Reionization Arrays (HERA[4]; DeBoer et al. 2017) and the Square Kilometre Array (SKA[5]), which promise to deliver three-dimensional imaging and a high S/N measurement of the 21-cm PS out to $z \lesssim 20$–30.

However, even with a clean detection of the signal, it is not obvious that we can claim to have detected MCGs. Given how little we know about high-redshift galaxies, there could be many degeneracies in theoretical models. *Would we be able to confidently extract the imprint of MCGs from the signal, and distinguish them from more evolved, second-generation galaxies?* Bayesian inference provides us with a clean framework to answer such a question. Specifically, Bayesian evidence allows us to perform model selection, quantifying if data prefers one theoretical model over another. It has a built-in Occam's razor factor, penalizing additional model complexity unless explicitly required by the data (for a recent review of Bayesian inference in astronomy, see Trotta 2017).

In this work, we quantify the detectability of MCGs from a mock measurement of the cosmic 21-cm PS, expected from a 1000 h integration with SKA1-low. Our mock signal is generated by self-consistently following the evolution of both MCGs and more massive atomically cooled galaxies (ACGs), as described in Qin et al. (2020, hereafter Paper-I). From this mock observation, we infer the properties of the underlying galaxies using a model having only a population of ACGs, and a model allowing for both populations: ACGs and MCGs. We compute the Bayes factor of these two models, quantifying if the mock observation provides sufficient evidence for an additional population of MCGs.

This paper is organized as follows. We briefly summarize our model in Section 2. In Section 3, we present our mock observation, chosen so that the timing of the global signal is consistent with the putative EDGES detection. In Section 4, we perform parameter inference using two galaxy models, presenting the corresponding Bayesian evidence. Finally, we conclude in Section 5. In this work, we adopt the following cosmological parameters: $\Omega_{\rm m}$, $\Omega_{\rm b}$, Ω_Λ, h, σ_8, $n_{\rm s} = 0.31, 0.048, 0.69, 0.68, 0.81, 0.97$, consistent with *Planck* (Planck Collaboration XIII 2016b; Planck Collaboration VI 2018).

2 CHARACTERIZING GALAXIES AT COSMIC DAWN

To model the 21-cm signal we use the public code 21cmFAST[6] (Mesinger & Furlanetto 2007; Mesinger, Furlanetto & Cen 2011) with the latest update from Paper-I. In Paper-I, we extended the galaxy models of 21cmFAST to include a separate population of MCGs, with properties independent to those of ACGs. Here, we briefly summarize our procedure for characterizing these galaxies and their corresponding emissivities; for more details, see Paper-I.

We define two distinct galaxy populations on the basis of the cooling channel through which they obtained the bulk of their gas – ACGs and MCGs. These two populations are defined via exponential 'window functions' over the halo mass ($M_{\rm h}$) function, dn/d$M_{\rm h}$ (for an in-depth discussion of this choice, see Paper-I). Specifically, the number density of actively star-forming galaxies is

$$\phi = \frac{{\rm d}n}{{\rm d}M_{\rm h}} \times \begin{cases} \exp\left(-\dfrac{M_{\rm crit}^{\rm atom}}{M_{\rm h}}\right) \\ \exp\left(-\dfrac{M_{\rm crit}^{\rm mol}}{M_{\rm h}}\right) \exp\left(-\dfrac{M_{\rm h}}{M_{\rm crit}^{\rm cool}}\right) \end{cases} , \tag{1}$$

where the superscripts 'atom' and 'mol' are used to distinguish ACGs and MCGs, respectively, as they are allowed to have different properties and scaling relations.

We see from equation (1) that the occupancy fraction of ACGs starts dropping below a characteristic mass scale of

$$M_{\rm crit}^{\rm atom} = \max\left[M_{\rm crit}^{\rm cool}, M_{\rm crit}^{\rm ion}, M_{\rm crit}^{\rm SN}\right] . \tag{2}$$

Here, we account for three physical processes that can suppress star formation: (i) inefficient cooling, $M_{\rm crit}^{\rm cool}$ (corresponding to a virial temperature of $\sim 10^4$ K; Barkana & Loeb 2001); (ii) photoheating feedback from inhomogeneous reionization, $M_{\rm crit}^{\rm ion}$ (e.g. Sobacchi & Mesinger 2014; see also Efstathiou 1992; Shapiro, Giroux & Babul 1994; Thoul & Weinberg 1996; Hui & Gnedin 1997); and (iii) supernova feedback,[7] $M_{\rm crit}^{\rm SN}$ (Haiman et al. 2000; Wise & Abel 2007; Dalla Vecchia & Schaye 2008, 2012; Hopkins et al. 2014, 2018; Keller et al. 2014; Kimm et al. 2017).

On the other hand, the occupancy fraction of MCGs picks up below the atomic cooling threshold, $M_{\rm crit}^{\rm cool}$, and extends down to

$$M_{\rm crit}^{\rm mol} = \max\left[M_{\rm crit}^{\rm diss}, M_{\rm crit}^{\rm ion}, M_{\rm crit}^{\rm SN}\right] , \tag{3}$$

where the additional term, $M_{\rm crit}^{\rm diss}$, accounts for the cooling efficiency of H_2 in the presence of an inhomogeneous LW background (e.g. Draine & Bertoldi 1996; Machacek, Bryan & Abel 2001; Johnson et al. 2007; Ahn et al. 2009; Wolcott-Green, Haiman & Bryan 2011;

[1] http://www.lofar.org/
[2] http://www.mwatelescope.org/
[3] http://eor.berkeley.edu
[4] http://reionization.org/
[5] https://www.skatelescope.org/

[6] https://github.com/21cmfast/21cmFAST
[7] Following Paper-I, here we also assume $M_{\rm crit}^{\rm SN}$ is smaller than the other relevant mass scales, so that we can maximize the importance of MCG and thus match the timing of the putative EDGES detection. Note that SNe feedback could still be responsible for the power-law scaling of the stellar to halo mass relation if star formation is feedback limited (e.g. Wyithe & Loeb 2013).

Holzbauer & Furlanetto 2012; Visbal et al. 2015). It is worth noting that metal enrichment from nearby star-forming haloes can impact the cooling function for some clustered galaxies; however, we do not consider this here as such cases are expected to be very rare (e.g. Wise et al. 2012; Visbal, Haiman & Bryan 2018; Liu & Bromm 2020; Nakatani, Fialkov & Yoshida 2020).

We adopt power-law relations for the stellar (M_*) to halo mass ratio (Moster, Naab & White 2013; Mutch et al. 2016; Sun & Furlanetto 2016; Ma et al. 2018; Tacchella et al. 2018; Behroozi et al. 2019; Yung et al. 2019)

$$\frac{M_*}{M_\mathrm{h}} = \frac{\Omega_\mathrm{b}}{\Omega_\mathrm{m}} \times \min\left[1, \begin{cases} f_{*,10}^{\mathrm{atom}} \left(\frac{M_\mathrm{h}}{10^{10}\mathrm{M}_\odot}\right)^{\alpha_*} \\ f_{*,7}^{\mathrm{mol}} \left(\frac{M_\mathrm{h}}{10^{7}\mathrm{M}_\odot}\right)^{\alpha_*} \end{cases}\right], \quad (4)$$

where three free parameters ($f_{*,10}^{\mathrm{atom}}$, $f_{*,7}^{\mathrm{mol}}$, and α_*) set the normalizations and scaling index.

We assume that the stellar mass is on average built-up over some fraction of the Hubble time, $t_* H(z)^{-1}$, resulting in a star formation rate of SFR $= M_* H(z)/t_*$. Here, for computational convenience, we fix $t_* = 0.5$ (corresponding to $\sim$ few times the halo dynamical time), noting that there is a strong degeneracy between f_* and t_*, and the prior distribution over these two parameters results in a relative insensitivity of the results to t_* (Park et al. 2019; Paper-I). To compare with observed UV LFs (e.g. Bouwens et al. 2015, 2016; Finkelstein et al. 2015; Livermore, Finkelstein & Lotz 2017; Atek et al. 2018; Oesch et al. 2018; Bhatawdekar et al. 2019), we also compute the corresponding 1500 Å; luminosity with a conversion factor $L_{1500}/\mathrm{SFR} = 8.7 \times 10^{27} \mathrm{erg\,s^{-1}\,Hz^{-1}\,yr}$ (Madau & Dickinson 2014).

We allow ACGs and MCGs to have different UV ionizing escape fractions, also with power-law scalings with halo mass. However, for computational convenience, here we assume no evolution with halo mass or redshift resulting in just two additional free parameters, $f_{\mathrm{esc}}^{\mathrm{atom}}$ and $f_{\mathrm{esc}}^{\mathrm{mol}}$).

The dominant sources of X-rays in the very early Universe are expected to be high-mass X-ray binaries (HMXBs; Sanderbeck et al. 2018). Motivated by models and observations of HMXBs (e.g. Mineo, Gilfanov & Sunyaev 2012; Fragos et al. 2013; Pacucci et al. 2014), we assume their population-averaged specific X-ray luminosity scales linearly with the SFR of host galaxies, and has a power-law SED with an energy spectral index of -1. We assume that only X-rays with energy greater than $E_0 = 500$ eV can escape the host galaxy and interact with the IGM. This value is motivated by high-resolution hydrodynamic simulations of the ISM in the first galaxies (Das et al. 2017). Moreover, we characterize the X-ray luminosity of early galaxies with their *soft-band* (<2keV) X-ray luminosities, as harder photons have a mean free path longer than the Hubble length and thus do not interact with the IGM. In other words, the specific X-ray luminosity is described by

$$\frac{\mathrm{d}L_{\mathrm{X}/\odot}}{\mathrm{d}E} = \frac{E^{-1}}{\int_{500\,\mathrm{eV}}^{2\,\mathrm{keV}} \mathrm{d}E\, E^{-1}} \times \begin{cases} L_{\mathrm{X<2\,keV}/\odot}^{\mathrm{atom}} \\ L_{\mathrm{X<2\,keV}/\odot}^{\mathrm{mol}} \end{cases}, \quad (5)$$

where we include two more free parameters (i.e. $L_{\mathrm{X<2\,keV}/\odot}^{\mathrm{atom}}$ and $L_{\mathrm{X<2\,keV}/\odot}^{\mathrm{mol}}$) as the total soft-band luminosity per SFR for ACGs and MCGs.

Based on these galaxy properties, we can calculate (1) the ionization and heating rates by X-rays; (2) the Lyman α coupling coefficient between the IGM spin and kinetic temperatures; (3) the LW radiation intensity and the critical halo mass characterizing the radiative feedback from LW suppression; as well as (4) the UV ionizing photon budget and the critical mass for photoheating feedback (see equation 1). It is worth noting that we also include inhomogeneous recombinations (Sobacchi & Mesinger 2014), adopting a sub-grid density distribution from Miralda-Escudé, Haehnelt & Rees (2000) but adjusted for the mean density in each cell, and account for density-dependent attenuation of the local ionizing background according to (Rahmati et al. 2013). These quantities are then used to follow the temperature and ionization state of each gas element in our simulation, which are in turn used to compute the 21-cm signal. For more details, see Mesinger et al. (2011) and Paper-I.

3 MOCK 21-CM OBSERVATION

We create a mock 21-cm observation from a simulation box with a comoving volume of $(500\,\mathrm{Mpc})^3$ and a 256^3 grid. While the full parameter space of our model is very large (17 dimensional; see table 1 in Paper-I), in this proof-of-concept work, we limit it to the seven parameters[8] that drive the largest signal variation and are most relevant for the early Cosmic Dawn signal. These include $f_{*,10}^{\mathrm{atom}}$, $f_{*,10}^{\mathrm{mol}}$, α_*, $f_{\mathrm{esc}}^{\mathrm{atom}}$, $f_{\mathrm{esc}}^{\mathrm{mol}}$, $L_{\mathrm{X<2\,keV}/\odot}^{\mathrm{atom}}$, and $L_{\mathrm{X<2\,keV}/\odot}^{\mathrm{mol}}$. Table 1 summarizes their physical meaning, and shows the fiducial values we use to make our mock observation. These fiducial values are chosen in order for the mock observation to be consistent with the following observations:

(i) the galaxy UV LFs at $z \sim 6-10$ (Bouwens et al. 2015, 2016; Oesch et al. 2018);

(ii) the upper limit on the neutral fraction at $z \sim 5.9$ from the dark fraction in QSO spectra ($x_{\mathrm{HI}} < 0.06 + 0.05$, 1σ; McGreer, Mesinger & D'Odorico 2015);

(iii) the CMB Thomson scattering optical depth from *Planck* ($\tau_e = 0.058 \pm 0.012$, 1σ; Planck Collaboration XLVII 2016a); and

(iv) the timing[9] of the recent putative detection of an absorption profile centred at 78 $\pm$ 1MHz in the global 21-cm spectrum by EDGES (Bowman et al. 2018).

We note that, $f_{*,10}^{\mathrm{atom}}\sim$6 per cent and $\alpha_* = 0.5$ are already well constrained by the observed high-redshift UV LFs while $f_{\mathrm{esc}}^{\mathrm{atom}}$=6 per cent ensures reionization of the fiducial model finishes by $z \sim 5.9$, with the inferred τ_e consistent with results from *Planck*. On the other hand, $\log_{10}\left[L_{\mathrm{X<2\,keV}/\odot}^{\mathrm{atom}}/\mathrm{erg\,s^{-1}\,M_\odot{}^{-1}\,yr}\right] = 40.5$ is motivated by theoretical models of HMXBs in metal-poor environments (Fragos et al. 2013). Without much knowledge of the MCG properties, we assume that their stellar to halo mass relation and escape fraction follow ACGs, and choose $f_{*,7}^{\mathrm{mol}}\sim$0.2 per cent and $f_{\mathrm{esc}}^{\mathrm{mol}}$=6 per cent. Finally, an enhanced X-ray luminosity of MCGs, here we take $\log_{10}\left[L_{\mathrm{X<2\,keV}/\odot}^{\mathrm{atom}}/\mathrm{erg\,s^{-1}\,M_\odot{}^{-1}\,yr}\right] = 41.7$,

[8]The 7-parameter MULTINEST light-cone sampler presented in Section 4 cost 500 000 CPU h on the Australian national supercomputing facility, OzSTAR. We are actively developing the simulation (i.e. code optimization and new physics) to include further parameters including α_{esc}, E_0, and $M_{\mathrm{crit}}^{\mathrm{SN}}$ (see Table 1) as well as cosmological parameters such as σ_8.

[9]We only consider the timing from EDGES that is expected to be driven by minihaloes (see Paper-I and also Mirocha & Furlanetto 2019). This allows us to select an optimistic model for our proof-of-concept study, in which minihaloes play an important role. The amplitude of the reported signal cannot be explained by standard physics (e.g. Ewall-Wice et al. 2018; Fialkov et al. 2018; Muñoz & Loeb 2018; Mebane et al. 2020), and some exotic explanations could have a large impact also on the PS. However, *partial* degeneracy with unidentified systematics and/or foregrounds (e.g. Hill & Baxter 2018; Spinelli, Bernardi & Santos 2018; Bradley et al. 2019; Sims & Pober 2019) could bring the amplitude in line with standard models, without evoking exotic physics. Our mock PS corresponds to such a scenario.

Table 1. A list of the free parameters varied in this work, together with their descriptions, fiducial values used for the mock observation, and the recovered values (median with [14, 86] percentiles) obtained from the two 21CMMC runs. Other model parameters are held constant, using the values discussed in the text and in Paper-I. They are shown here for completeness and indicated by the † symbol.

Parameters	Description	Mock	21CMMC results	
			2pop	*1pop*
$\log_{10} f_{*,10}^{\rm atom}$	Stellar to halo mass ratio at $M_{\rm vir} = 10^{10}{\rm M}_\odot$ for ACGs	-1.25	$-1.28^{+0.05}_{-0.19}$	$-1.28^{+0.06}_{-0.24}$
$\log_{10} f_{*,7}^{\rm mol}$	Stellar to halo mass ratio at $M_{\rm vir} = 10^{7}{\rm M}_\odot$ for MCGs	-2.75	$-3.08^{+0.89}_{-0.61}$	–
α_*	Stellar to halo mass power-law index	0.5	$0.52^{+0.16}_{-0.11}$	$0.43^{+0.27}_{-0.09}$
$t_*^\dagger$	Star formation time-scale in units of the Hubble time	0.5	–	–
$\log_{10} f_{\rm esc}^{\rm atom}$	Escape fraction of ionizing photons for ACGs	-1.22	$-1.23^{+0.14}_{-0.21}$	$-1.14^{+0.12}_{-0.14}$
$\log_{10} f_{\rm esc}^{\rm mol}$	Escape fraction of ionizing photons for MCGs	-1.22	$-1.38^{+0.93}_{-1.05}$	–
$\alpha_{\rm esc}^{\rm atom\,\dagger}$	Escape fraction of ionizing photons to halo mass power-law indices for ACGs	0	–	–
$\alpha_{\rm esc}^{\rm mol\,\dagger}$	Escape fraction of ionizing photons to halo mass power-law indices for MCGs	0	–	–
$n_\gamma^{\rm atom\,\dagger}$	Number of ionizing photons emitted per stellar baryon for ACGs	5×10^3	–	–
$n_\gamma^{\rm mol\,\dagger}$	Number of ionizing photons emitted per stellar baryon for MCGs	5×10^4	–	–
$\alpha_{\rm UVB}{}^\dagger$	Spectral index of the ionizing background	5	–	–
$\log_{10} L_{\rm X<2\,keV/\odot}^{\rm atom}$	Soft-band X-ray luminosity per SFR (erg s^{-1} M$_\odot^{-1}$ yr) for ACGs	40.5	$40.64^{+1.28}_{-1.88}$	$41.21^{+1.17}_{-0.22}$
$\log_{10} L_{\rm X<2\,keV/\odot}^{\rm mol}$	Soft-band X-ray luminosity per SFR (erg s^{-1} M$_\odot^{-1}$ yr) for MCGs	41.7	$41.77^{+1.07}_{-2.01}$	–
$E_0^\dagger$	Minimum X-ray energy escaping the galaxies into the IGM	500 eV	–	–
$\alpha_{\rm X}^\dagger$	Spectral index of X-ray sources	1	–	–
$M_{\rm crit}^{\rm SN\,\dagger}$	Critical halo mass for supernova feedback $\leq \max\left(M_{\rm crit}^{\rm cool}, M_{\rm crit}^{\rm ion}\right)$		–	–
$f_{\rm H2}^{\rm shield\,\dagger}$	Self-shielding factor of H_2 for LW dissociation	0	–	–

is needed[10] to reproduce an 21-cm absorption trough centred at ∼78 MHz (Paper-I). This could be motivated by more luminous X-ray binaries arising from Pop-III stellar remnants in MCGs (Xu et al. 2016a). It is important to note that these are just fiducial parameter values, chosen to make the mock observation consistent with our current knowledge; there are large uncertainties and strong degeneracies as we will see below.

We present the 21-cm light-cone from our fiducial model in the upper panel of Fig. 1 and show its globally averaged 21-cm brightness temperature evolution, EoR history as well as the Thomson scattering optical depth ($\tau_e = 0.062$) in the upper right three sub-panels of Fig. 2 using black solid curves. We see that the model is consistent with the aforementioned observational constraints. The signal follows the expected qualitative trends (e.g. Furlanetto, Oh & Briggs 2006; Baek et al. 2010; Santos et al. 2011; Mesinger, Greig & Sobacchi 2016; Park et al. 2019). During the Cosmic Dawn, the first galaxies begin to build up the Lyman α background, coupling the spin ($T_{\rm s}$) and kinetic temperatures ($T_{\rm k}$). The brightness temperature ($\delta T_{\rm b}$) is negative (i.e. the IGM is seen in absorption against the CMB) and decreases as the IGM adiabatically cools faster than the CMB. For our choice of galaxy parameters, $\delta T_{\rm b}$ reaches its minimum at $z \sim 17$, before X-ray heating becomes significant, eventually heating the IGM to temperatures above the CMB by $z \sim 13-14$. As reionization progresses, the signal starts fading until $z \sim 5.8$ when the universe is fully ionized (apart from the residual H I).

3.1 Synthetic power spectra and telescope noise

Following Greig & Mesinger (2018), we compress the cosmic 21-cm light-cone into 3D averaged power spectra. The PS from the mock observation (generated from a unique initial seed) and the forward-modelled simulations (in Section 4) are calculated from the same comoving volume of the light-cone. For computing efficiency, forward-modelled simulations have a factor of 2^3 smaller volume than the mock while keeping the same resolution, i.e. $(250\,{\rm Mpc})^3$ and 128^3 cells. Therefore, we compute the PS from 12 independent sub volumes of the light-cone between $z = 5.5$ (∼220 MHz) and $z = 30$ (∼50 MHz). The resulting 3D-averaged PS are shown with the black curves in the sub-panels of Fig. 1, with the central redshifts indicated in the top left of each panel and with the vertical lines in the top panel.

We add to our cosmic 21-cm PS instrument noise corresponding to a 1000 h integration with SKA1-low.[11] We use the public

[10] This is based on the strong degeneracy between $f_{*,7}^{\rm mol}$ and the X-ray luminosity per SFR found in Paper-I ($\log_{10} f_{*,7}^{\rm mol} + \log_{10} \frac{L_{\rm X<2\,keV/\odot}}{\rm erg\ s^{-1}\ M_\odot^{-1}\ yr} = 38.92^{+0.24}_{-0.15}$). Note that although ACGs and MCGs are assumed to share the same specific X-ray luminosity in Paper-I, a smaller $L_{\rm X<2\,keV/\odot}^{\rm atom}$ used in this work does not have a significant impact to the timing of the absorption trough because the contribution from ACGs at high redshifts ($z \gtrsim 15$) is small. It is also worth noting that our conclusion on the detectability of minihaloes remains valid for other models where minihalo-hosted galaxies truly play a significant role and their properties follow the aforementioned relation.

[11] Note that HERA is expected to provide comparable astrophysical parameter recovery as SKA1-low, using the PS summary statistic and the fiducial galaxy models from Park et al. (2019) and Greig, Mesinger & Koopmans (2020). However, our fiducial model here is chosen to have a significant contribution of MCGs driving a much earlier epoch of heating, as motivated by the putative EDGES detection. As thermal noise dominates at the corresponding low frequencies and SKA1-low should have smaller thermal noise than HERA

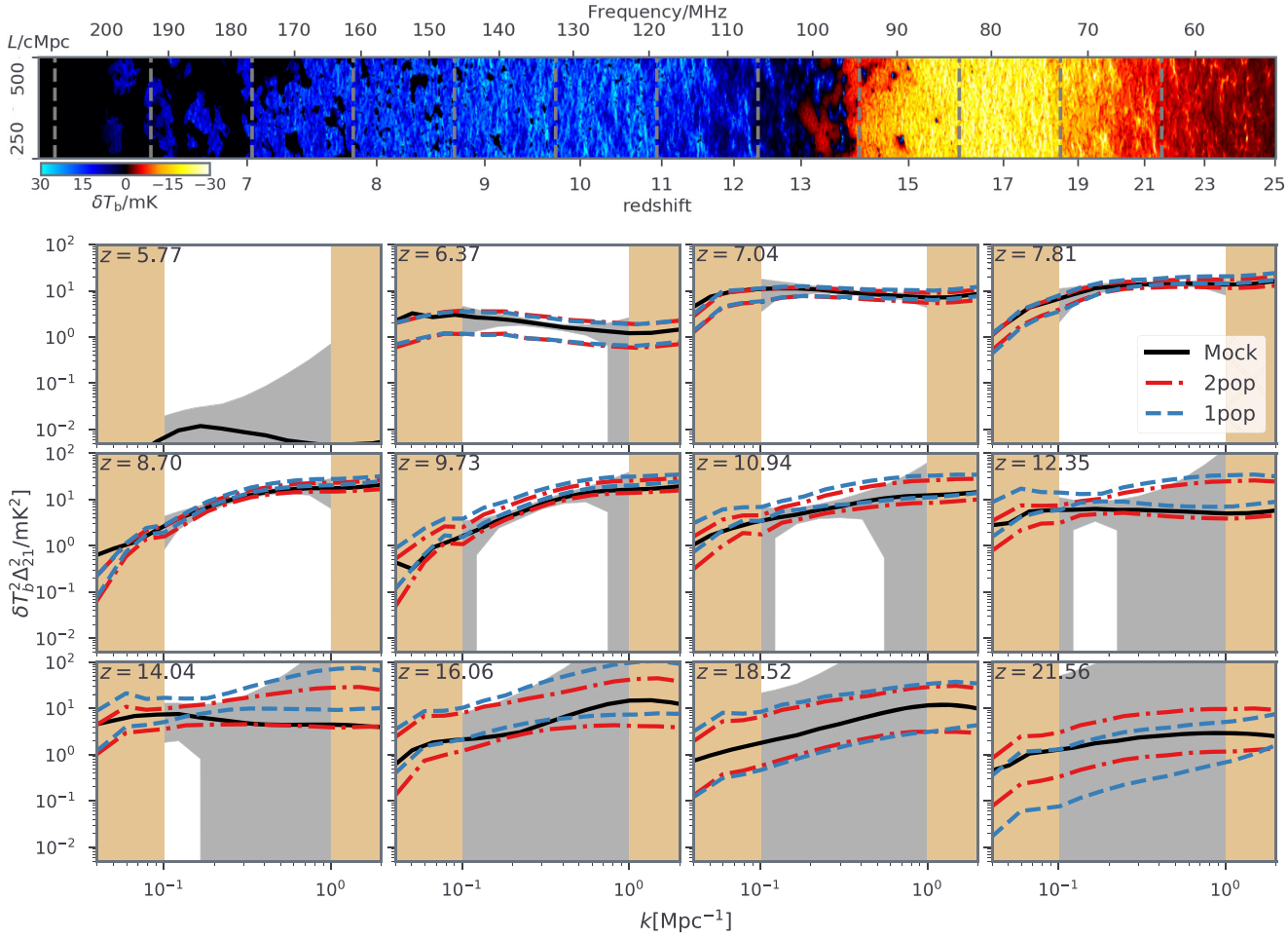

Figure 1. *Top panel*: A slice of the 21-cm light-cone from our mock observation. The central redshifts of the 12 independent box samples, which are used to calculate the 21-cm PS, are indicated by the vertical dashed lines. Note that the spatial range of the vertical axis is from 250 to 500 cMpc, half the entire light-cone length (500 cMpc). *Lower panels:* Evolution of the 21-cm PS. Solid black curves correspond to the mock observation, with grey shaded regions indicating the 1σ noise from a 1000 h observation with SKA1-low. Only power within the range of $k = 0.1$–$1\,\mathrm{Mpc}^{-1}$ is considered when performing the Bayesian inference. The [14, 86] percentiles of the recovered posteriors from Fig. 2 are bracketed by the coloured lines (*2pop* using red dash–dotted lines, *1pop* using blue dashed lines).

21CMSENSE package (Pober et al. 2013, 2014). We adopt the 'moderate' foreground removal configuration, which excises foreground contaminated modes from the cylindrical k-space 'wedge' (which is assumed to extend at $k_{\parallel} \approx 0.1\,h\,\mathrm{Mpc}^{-1}$ above the horizon limit) and assumes coherent addition of only instantaneously redundant baselines (see more in Pober et al. 2014). We provide a brief summary of the relevant calculations here and direct interested readers to the aforementioned papers for more details.

The thermal noise PS of a single baseline corresponding to a given k mode is (Morales 2005; McQuinn et al. 2006; Parsons et al. 2012)

$$\Delta^2_{\mathrm{N}}(k) \approx \frac{3k^3(1+z)^4}{2\pi^2\sqrt{\Omega_{\mathrm{m}}(1+z)^3+\Omega_{\Lambda}}}\Omega B T^2_{\mathrm{N}}, \tag{6}$$

where Ω and B correspond to the solid angle of the primary beam size (e.g. $\sim$0.1sr at $z = 17$) and observing bandwidth (8 MHz), respectively. We use the SKA1-low antennae configuration described in Greig et al. (2020). The system temperature is taken to be T_{N} $= (T_{\mathrm{sky}} + T_{\mathrm{rec}})(2Bt)^{-0.5}$ where T_{sky} and T_{rec} represent the sky and receiver temperatures while the factor, $\sqrt{2Bt}$, reflects the number of independent measurements during the integration time, t. Following Thompson, Moran & Swenson (2017), the sky is modelled as being dominated by Galactic synchrotron emission and scales with frequency (ν) as $T_{\mathrm{sky}} = 60\,\mathrm{K}(\nu/300\,\mathrm{MHz})^{-2.55}$. On the other hand, the receiver is assumed to be kept at 40K with an addition of $0.1T_{\mathrm{sky}}$ reflecting its response to the sky (Pober et al. 2014).

The total uncertainty on the 21-cm PS ($\sigma\Delta^2_{21}$) is obtained by summing over the individual modes, i, (Pober et al. 2013), and adding the cosmic variance of the mock observation (reasonably assuming it is Gaussian distributed at the relevant scales; Mondal, Bharadwaj & Majumdar 2016, see also Shaw, Bharadwaj & Mondal 2019):

$$\left[\frac{1}{\sigma\Delta^2_{21}(k)}\right]^2 = \sum_i \left(\frac{1}{\Delta^2_{\mathrm{N,i}}+\Delta^2_{21}}\right)^2. \tag{7}$$

The grey shaded regions in Fig. 1 show the resulting 1σ uncertainty on the mock cosmic signal. We note large uncertainties at high redshifts while most constraints from the 21-cm PS come from large scales and $z < 15$. When performing inference, we additionally

for a fixed integration time, for this proof-of-concept study we make the slightly more optimistic choice of SKA1-low when computing the noise.

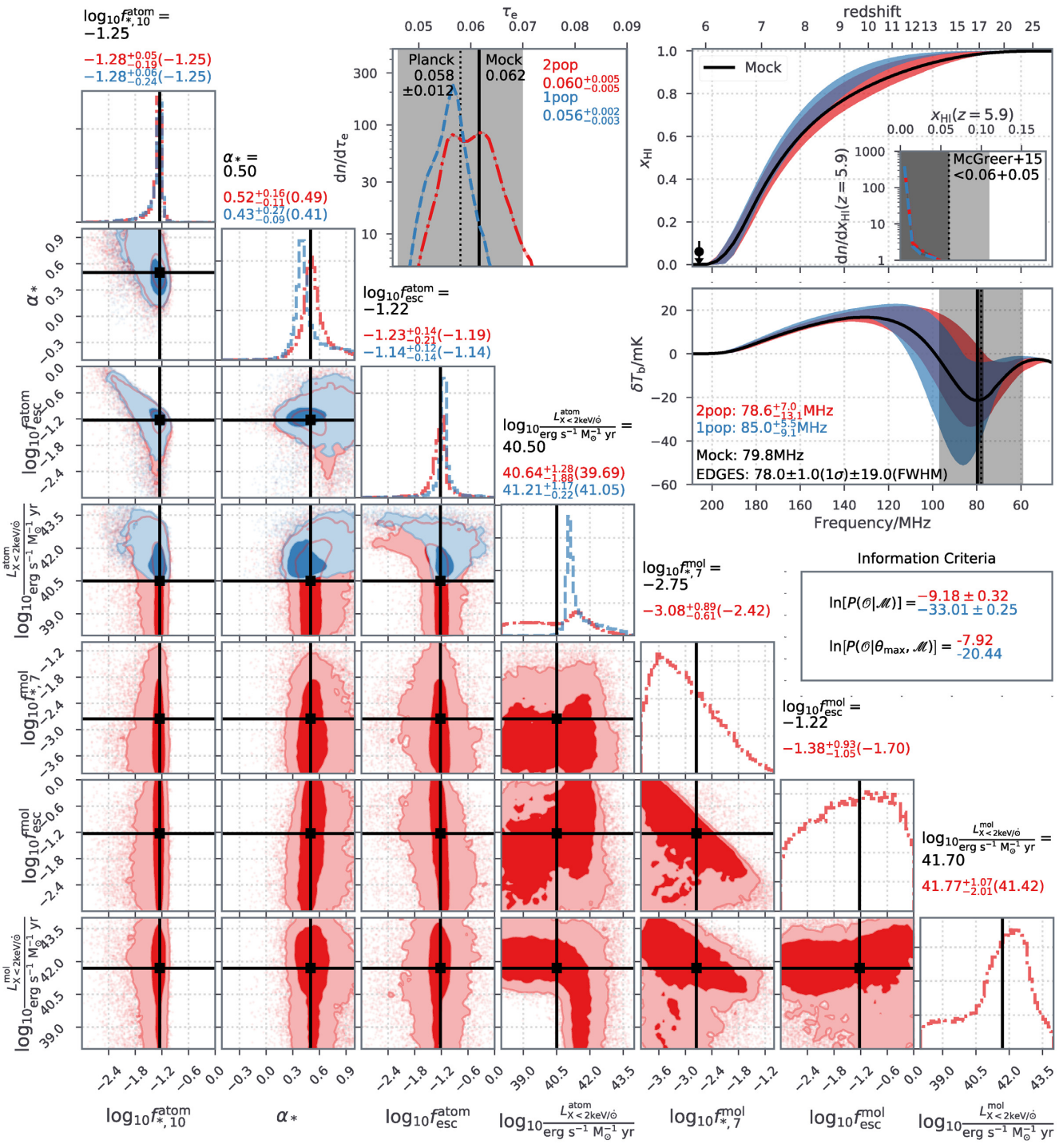

Figure 2. Marginalized posterior distributions from our two astrophysical models: (i) *2pop* in red/dash–dotted lines; (ii) *1pop* in blue/dashed lines. While the *1pop* model only considers four parameters describing ACGs, *2pop* includes additional three parameters representing the properties of MCGs. Both results use the following observations when computing the likelihood: (i) the observed galaxy LFs at $z \sim 6-10$ (Bouwens et al. 2015, 2016; Oesch et al. 2018); (ii) the upper limits on the neutral fraction at $z \sim 5.9$ from QSO spectra (McGreer et al. 2015); (iii) the Thomson scattering optical depth of the CMB (Planck Collaboration XLVII 2016a); and (iv) the 21-cm power spectra from a mock observation (chosen to be consistent with timing implied by the putative EDGES detection; Bowman et al. 2018; see the black solid lines in Fig. 1). The 2D distributions correspond to 68th (dark regions) and 95th (light regions) percentiles. The medians with [14, 86] percentiles for each parameter are presented on the top of the 1D PDF together with the values for the maximum likelihood models (in brackets). The mock parameters are indicated by solid black lines in the posterior with their values shown on the top of the 1D PDFs as well. The upper right three sub-panels present the [14, 86] percentiles of the volume weighted neutral hydrogen fraction ($x_{\rm H\,I}$) and brightness temperature ($\delta T_{\rm b}$) as well as the PDF of τ_e and $x_{\rm H\,I}$ at $z = 5.9$ for the two posterior distributions. Fiducial values from the mock observation are denoted with solid black curves. Observations are indicated in grey or using black circles.

exclude the modes outside the range $0.1 \leq k/\mathrm{Mpc}^{-1} \leq 1$ (demarked in brown in the panels). This is done to conservatively avoid additional foreground contamination as well as aliasing (shot noise) effects from our simulation grids. Moreover, we add an additional 20 per cent 'modelling error' to our forward-modelled PS, roughly motivated by comparisons to radiative transfer simulations (e.g. Zahn et al. 2011). We note however that such modelling error is unlikely to have a major impact on parameter inference (Greig et al. 2020).

4 CAN WE INDIRECTLY DETECT THE FIRST, MOLECULARLY COOLED GALAXIES?

In this section, we use 21CMMC (Greig & Mesinger 2015) to constrain astrophysical parameters and perform model selection using the following observations:

(i) the mock 21-cm power spectra discussed in Section 3.1;
(ii) the observed galaxy LFs at $z \sim 6-10$ (Bouwens et al. 2015, 2016; Oesch et al. 2018);
(iii) the upper limits on the neutral fraction at $z \sim 5.9$ from QSO spectra (McGreer et al. 2015); and
(iv) the Thomson scattering optical depth of the CMB (Planck Collaboration XLVII 2016a).

We perform inference using the following two models:

(i) *2pop*: the 'full' model, including both MCGs and ACGs, used to generate the mock observation; and
(ii) *1pop*: a single population model consisting only of ACGs.

2pop is characterized with the seven free parameters listed in Table 1, while *1pop* only has the four parameters relevant for ACGs (i.e. excluding the ones labelled 'mol'). It is clear that *1pop* cannot fully reproduce the mock observation: ACGs are too biased at early times and are not sensitive to the build-up of the inhomogeneous LW background. However, given the limited sensitivity of even SKA1-low during the Cosmic Dawn, will we be able to say with certainty that the *1pop* model is incorrect?

This question can be readily answered with Bayesian inference. Using the built-in Occam's razor in the Bayes factor, we can quantify whether the unique properties of MCGs are needed to explain the 'observation', or whether the simpler, single-population model can adequately mimic the signal. Is the additional model complexity of *2pop* justified by the data? If not, we might not be able to detect minihalo galaxies even indirectly with upcoming interferometers.

Before presenting our results in Section 4.3, we briefly review the basics of Bayesian model selection (Section 4.1), as well as the MULTINEST sampler we use inside 21CMMC (Section 4.2).

4.1 Bayesian evidence and model selection

Bayes' law states that the posterior probability distribution $[P(\theta|\mathscr{O}, \mathscr{M})]$ of model ($\mathscr{M}$) characterized by parameters (θ) when constrained by observations ($\mathscr{O}$) is equal to the product of our prior knowledge $[P(\theta|\mathscr{M})]$ and the likelihood function $[P(\mathscr{O}|\theta, \mathscr{M})]$ divided by the evidence $[P(\mathscr{O}|\mathscr{M})]$

$$P(\theta|\mathscr{O}, \mathscr{M}) = P(\theta|\mathscr{M})\frac{P(\mathscr{O}|\theta, \mathscr{M})}{P(\mathscr{O}|\mathscr{M})}. \tag{8}$$

While the posterior represents our belief about the model after taking the observation into account, the prior reflects our knowledge before.[12] The likelihood measures how well a parameter combination θ can reproduce the observed data $\mathscr{O}$.

The Bayesian evidence, also known as the marginal likelihood, is central to model selection. It can be computed by integrating the likelihood, weighted by the prior, over the entire parameter space:

$$\begin{aligned} P(\mathscr{O}|\mathscr{M}) &= \oint_\theta \mathrm{d}\theta\, P(\mathscr{O}|\theta, \mathscr{M})P(\theta|\mathscr{M}) \\ &\sim \delta\theta\, P(\mathscr{O}|\theta_{\max}, \mathscr{M})P(\theta_{\max}|\mathscr{M}). \end{aligned} \tag{9}$$

The last step in equation (9) approximates the integral trapezoidally around the maximum likelihood, $P(\mathscr{O}|\theta_{\max}, \mathscr{M})$ (e.g. Trotta 2017). Here, $\delta\theta$ and $\Delta\theta \equiv P^{-1}(\theta_{\max}|\mathscr{M})$ characterize widths of the likelihood and prior, respectively. The factor $\delta\theta/\Delta\theta$ is commonly referred to as Occam's factor, as it penalizes models which have a prior volume that is larger than the likelihood.

There are many model selection criteria (Liddle 2004, 2007) to answer whether the increased complexity (see more in Kunz, Trotta & Parkinson 2006) of a model involving a higher dimensional parameter space is justifiable by the observation – in our case, whether upcoming 21-cm PS measurements can be used to detect minihalo-hosted galaxies. Here, we use an empirical scale (Jeffreys 1939) based on the ratio of the evidences of the two models, the so-called Bayes factor. Specifically, the probability of the *2pop* model being preferred over *1pop* is 75.0 per cent (weak), 92.3 per cent (moderate), and 99.3 per cent (strong) if $\ln B \equiv \ln\left[P(\mathscr{O}|\mathscr{M}_{2pop})/P(\mathscr{O}|\mathscr{M}_{1pop})\right]$ is 1, 2.5, and 5, respectively.

4.2 Including MULTINEST in 21CMMC

21CMMC[13] (Greig & Mesinger 2015) is a Bayesian sampler of 21-cm light-cones, allowing for cosmological and astrophysical parameter inference from the 21-cm signal (Greig & Mesinger 2017, 2018). In its default configuration, 21CMMC employs an ensemble sampler (EMCEE; Goodman & Weare 2010; Akeret et al. 2013; Foreman-Mackey et al. 2013) to explore the parameter space, which does not require the evidence to generate a proposal distribution. This makes the evaluation of the Bayesian evidence computationally challenging in a high-dimensional parameter space (see the first part of equation 9).

In this work, we include the MULTINEST[14] sampler (Feroz & Hobson 2008; Feroz, Hobson & Bridges 2009; Buchner et al. 2014; Feroz et al. 2019) in 21CMMC, which implements nested sampling – converting the variable of integration in equation (9) from the high-dimensional parameter space to the 1D prior space (see more in Skilling 2004)

$$P(\mathscr{O}|\mathscr{M}) = \int_0^1 \mathrm{d}P(\theta|\mathscr{M})P[\mathscr{O}|P(\theta|\mathscr{M})], \tag{10}$$

where $\mathrm{d}P(\theta|\mathscr{M}) \equiv d\theta\, P(\theta|\mathscr{M})$ represents the differential of prior volume. By reducing the prior volume around higher probability regions at each step when new sampling points are drawn, MULTINEST

[12] Here, we use a flat prior over the following ranges: $f_{*,10}^{\mathrm{atom}} \in [10^{-3}, 1]$ in logarithmic space; $f_{*,10}^{\mathrm{mol}} \in [10^{-4}, 10^{-1}]$ in logarithmic space; $\alpha_* \in [-0.5, 1]$; $f_{\mathrm{esc}}^{\mathrm{atom(mol)}} \in [10^{-3}, 1]$ in logarithmic space; and $L_{\mathrm{X<2\,keV}/\odot}^{\mathrm{atom(mol)}} \in [10^{38}, 10^{44}]$ erg s^{-1} M$_\odot^{-1}$ yr in logarithmic space.

[13] https://github.com/21cmfast/21CMMC

[14] https://github.com/rjw57/MultiNest
https://github.com/JohannesBuchner/PyMultiNest

computes the posterior and calculates the Bayesian evidence as a 'by-product'. The current public version of 21CMMC allows the user to choose between EMCEE and MULTINEST samplers.

It is worth noting that the recent development of 21CMNEST by Binnie & Pritchard (2019) also introduced MULTINEST into 21CMMC. They found the posterior of a 3-parameter 21-cm model inferred from mock observations to be consistent between 21CMNEST and the original 21CMMC. This encourages us to apply it to our updated 21-cm simulations using more sophisticated galaxy models.

4.3 Strong evidence of minihaloes

In Fig. 2, we present the marginalized posteriors from our two models (*1pop*/*2pop* in blue/red), including model parameters, global 21-cm signals, EoR histories, and the optical depths. The corresponding 21-cm power spectra are shown in Fig. 1.

For both models, the properties of ACGs are tightly constrained, including $f_{*,10}^{\rm atom}$, α_*, and $f_{\rm esc}^{\rm atom}$. We caution however that these parameters, especially $f_{\rm esc}^{\rm atom}$, are *overconstrained* (e.g. compared to Park et al. 2019) due to the fact that several ACG parameters are kept fixed in this demonstrative study (most importantly $M_{\rm crit}^{\rm SN}$, $\alpha_{\rm esc}$, t_*).

In the absence of MCGs, we see that the *1pop* model dramatically overestimates the X-ray luminosities of ACGs, with the 1D PDF peaking sharply at $\log_{10}(L_{\rm X<2\,keV/\odot}^{\rm atom}/{\rm erg\ s^{-1}\ M_\odot^{-1}\ yr})\sim 41.0-42.4$: a factor of $\sim$3−75 times higher than the 'true' value of the mock signal. Moreover, the *1pop* model prefers a lower α_* (i.e. a steeper stellar mass function), despite the fact that the UV LFs already constrain this parameter (e.g. Park et al. 2019). Thus, the *1pop* posterior prefers galaxy models with more efficient star formation in lower mass haloes (i.e. smaller α_*) and with higher X-ray emissivities (i.e. larger $L_{\rm X<2\,keV/\odot}^{\rm atom}$), in order to (partially) compensate for the missing population of MCGs.

From the global evolution of the neutral fraction and brightness temperatures, as well as the power spectra, we see that the *1pop* model does indeed perform a reasonable job at capturing the mock observation. Differences emerge at the highest redshifts, when the radiation fields have a higher relative contribution from MCGs. Even with a higher X-ray emissivity and steeper stellar mass functions, the ACG-only model cannot fully capture the evolution of the ACG + MCG mock observation. ACGs are more biased galaxies, and are insensitive to LW feedback which can prolong the early evolution of IGM properties in feedback-dominated MCG models (e.g. Ahn et al. 2009; Holzbauer & Furlanetto 2012; Fialkov et al. 2013). Thus, compared to the mock signal, the *1pop* model has (i) a more rapid evolution of cosmic milestones and (ii) a higher 21-cm PS during the epochs when a single field (i.e. temperature or Lyα coupling) sources the fluctuations, thus making cross-terms negligible and allowing the 21-cm PS to be roughly estimated analogously to the halo model with a bias term for the galaxies (e.g. Pritchard & Furlanetto 2007; McQuinn & D'Aloisio 2018). Indeed, we see that the *1pop* model has a more rapid evolution of the early stages of reionization (see also Ahn et al. 2009). Moreover, during the epoch of heating when the 21-cm signal is sourced by temperature fluctuations ($12 \lesssim z \lesssim 15$), *1pop* prefers power spectra that are too high, and results in a too rapid evolution during the transition to the earlier, Lyα-dominated epoch ($z \gtrsim 15$).

On the other hand, the 'full', *2pop* model recovers the fiducial parameters of the mock observation quite well. The inferred global evolution of the neutral fraction and brightness temperature, as well as the power spectra, are all consistent with the mock observation, without any notable bias. The X-ray luminosity of MCGs is well constrained, to within $\sim$ 1 dex of the fiducial value. Interestingly, there is a tail in the PDF extending towards low luminosities. Looking at the $L_{\rm X<2\,keV/\odot}^{\rm atom}$–$L_{\rm X<2\,keV/\odot}^{\rm mol}$ marginalized posterior, we see that this is due to a partial degeneracy allowing ACGs to dominate the epoch of heating for those models in which MCGs do not emit significant soft X-rays.

The ionizing escape fraction of MCGs is poorly constrained, as they do not have a significant contribution to reionization. However, models with both high $f_{*,7}^{\rm mol}$ and $f_{\rm esc}^{\rm mol}$ are excluded as they would result in a Thomson scattering optical depth that is too high (see Paper-I; Visbal et al. 2015).

For completeness, we also present the marginalized UV LFs of ACGs, MCGs (only in *2pop*) and all galaxies in Fig. 3. We see that the ACGs and total LFs are tightly constrained at the bright end by currently available observations (Bouwens et al. 2015, 2016; Oesch et al. 2018). Compared to the mock observation, both *1pop* and *2pop* results are consistent at $M_{1500} < -8$. At fainter magnitudes, only the *2pop* model recovers the UV LFs, since MCGs dominate in this regime.

Finally, we come to the main question of this work: can we quantitatively claim that *2pop* is a better fit to the data, given that it has more free parameters compared to *1pop*? We quantify this using the Bayesian evidence: $\ln[P(\mathcal{O}|\mathcal{M})] = -9.18 \pm 0.32$ and -33.01 ± 0.25 for *2pop* and *1pop*, respectively. These result in a Bayes factor of $\ln B \equiv \ln\left[P(\mathcal{O}|\mathcal{M}_{2pop})/P(\mathcal{O}|\mathcal{M}_{1pop})\right] \sim 24$, suggesting the probability of *2pop* being preferred over *1pop* by the data (i.e. the mock 21-cm PS) is >99.3 per cent (Jeffreys 1939). We therefore conclude that the (mock) data require the additional parameters characterizing MCG (i.e. $f_{*,7}^{\rm mol}$, $f_{\rm esc}^{\rm mol}$, and $L_{\rm X<2\,keV/\odot}^{\rm mol}$). This means that it might be possible to indirectly detect the footprint of MCGs in upcoming 21-cm power spectra measurements. We caution that this conclusion is based on the assumption that minihalo-hosted galaxies truly play a significant role in the IGM evolution during the Cosmic Dawn (as would be the case if, for example, the EDGES detection is genuinely cosmological).

5 CONCLUSIONS

In this work, we quantify the detectability of minihaloes for upcoming 21-cm interferometers. We compute a mock 21-cm signal, motivated by the timing of the putative EDGES detection, which would be driven by X-ray luminous, molecularly cooled galaxies (Paper-I). The result additionally agrees with the observed high-redshift galaxy UV luminosity functions (Bouwens et al. 2015, 2016; Oesch et al. 2018), the upper limit on the neutral hydrogen fraction at $z \sim 5.9$ (McGreer et al. 2015), and the CMB optical depth from *Planck* satellite (Planck Collaboration XLVII 2016a). We calculate the 21-cm power spectra (PS) from this model, including telescope noise corresponding to a 1000-h integration with SKA1-low and -moderate foreground avoidance. These mock observations are then fed to the 21CMMC driver (Greig & Mesinger 2015), upgraded to allow for nested sampling (Feroz & Hobson 2008), and used to constrain two models: (i) *2pop*, including both MCGs and their massive atomic-cooling galaxy (ACG) counterparts and (ii) *1pop*, considering only ACGs.

We note that the *1pop* model is able to partially compensate for the missing population of MCGs by preferring a steeper stellar mass function (smaller α_*) and a more X-ray luminous population of HMXBs (higher $L_{\rm X<2\,keV/\odot}^{\rm atom}$). However, without a transient population of MCGs, the more biased galaxies in the *1pop* model result in a somewhat more rapid evolution of cosmic milestones, with a higher PS during the epoch of heating.

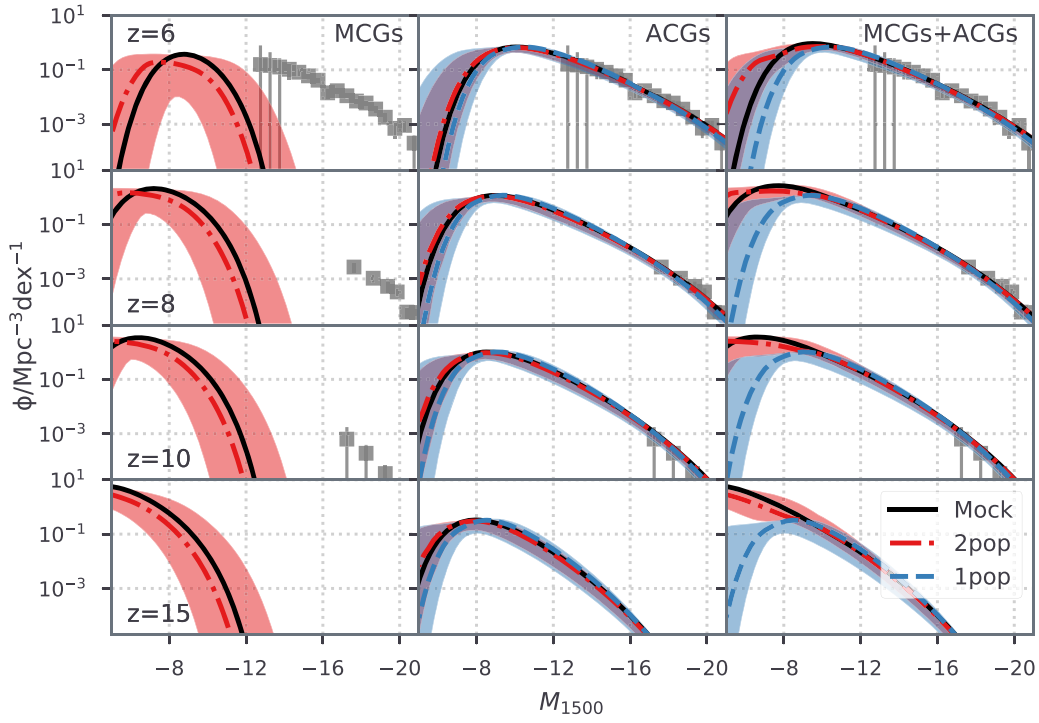

Figure 3. UV luminosity functions of MCGs, ACGs, and all galaxies from the model posteriors: (*2pop* in red, *1pop* in blue). Lines and shaded regions represent the median and [16, 84] percentiles. Observational estimates used in the inference (Bouwens et al. 2015, 2017; Oesch et al. 2018) are shown in grey at the bright end.

We quantify the preference of the mock observation for the more sophisticated galaxy model using the Bayesian evidence. We obtain $\ln[P(\mathcal{O}|\mathcal{M})] = -9.18 \pm 0.32$ and a maximum likelihood of $\ln[P(\mathcal{O}|\theta_{\rm max}, \mathcal{M})] = -7.92$ for *2pop*. These, compared to the *1pop* result (i.e. -33.01 ± 0.25 and -20.44), indicate a >99.3 per cent probability of *2pop* being preferred over *1pop* by the data (i.e. the mock 21-cm PS) according to the Jeffreys' scale (Jeffreys 1939). Thus, if minihalo-hosted galaxies indeed have a significant impact on high-redshift IGM properties (as would be the case if the timing of the EDGES signal is proven to be cosmological Bowman et al. 2018), we should be able to indirectly infer their existence and their properties from upcoming 21-cm observations.

More generally, our study showcases how upcoming 21-cm measurements can be used to discriminate against uncertain galaxy formation models, of varying complexity (see also Binnie & Pritchard 2019). Although we used two simplified, nested models here, the same analysis can be applied to even more sophisticated galaxy models (e.g. Moster et al. 2013; Mutch et al. 2016; Sun & Furlanetto 2016; Ma et al. 2018; Tacchella et al. 2018; Behroozi et al. 2019; Yung et al. 2019). Moreover, it can be used to statistically identify cosmological footprints, such as a large-scale modulation of MCG star formation rates due to the relative velocities of dark matter and baryons (e.g. Muñoz ; Schauer et al. 2019; Kulkarni, Visbal & Bryan 2020), as well as more exotic scenarios such as uniquely uniform heating through dark matter annihilation (e.g. Evoli, Mesinger & Ferrara 2014; Lopez-Honorez et al. 2016; Clark et al. 2018), cooling through dark matter–baryon interactions (e.g. Kovetz et al. 2018; Muñoz & Loeb 2018; Slatyer & Wu 2018), or accretion from primordial black holes (e.g. Ewall-Wice et al. 2018; Hektor et al. 2018; Mena et al. 2019). The need for additional complexity can be directly tested via the Occam's razor factor of the Bayesian evidence, by adding additional model parameters until the evidence is maximized.

ACKNOWLEDGEMENTS

The authors thank the anonymous referee for their comprehensive review and positive comments. This work was supported by the European Research Council (ERC) under the European Union's Horizon 2020 research and innovation programme (AIDA – #638809). The results presented here reflect the authors' views; the ERC is not responsible for their use. Parts of this research were supported by the Australian Research Council Centre of Excellence for All Sky Astrophysics in 3 Dimensions (ASTRO 3D), through project #CE170100013. This work was performed on the OzSTAR national facility at Swinburne University of Technology. OzSTAR is funded by Swinburne University of Technology and the National Collaborative Research Infrastructure Strategy (NCRIS). JP was supported in part by a KIAS individual Grant (PG078701) at Korea Institute for Advanced Study.

DATA AVAILABILITY

The data underlying this article will be shared on reasonable request to the corresponding author.

REFERENCES

Abel T., Bryan G. L., Norman M. L., 2002, Science, 295, 93
Ahn K., Shapiro P. R., Iliev I. T., Mellema G., Pen U.-L., 2009, ApJ, 695, 1430
Ahn K., Iliev I. T., Shapiro P. R., Mellema G., Koda J., Mao Y., 2012, ApJ, 756, L16
Akeret J., Seehars S., Amara A., Refregier A., Csillaghy A., 2013, Astron. Comput., 2, 27
Atek H., Richard J., Kneib J.-P., Schaerer D., 2018, MNRAS, 479, 5184
Baek S., Semelin B., Di Matteo P., Revaz Y., Combes F., 2010, A&A, 523, A4

Barkana R., Loeb A., 2001, Phys. Rep., 349, 125
Beardsley A. P. et al., 2016, ApJ, 833, 102
Beers T. C., Christlieb N., 2005, ARA&A, 43, 531
Behroozi P., Wechsler R. H., Hearin A. P., Conroy C., 2019, MNRAS, 488, 3143
Bhatawdekar R., Conselice C. J., Margalef-Bentabol B., Duncan K., 2019, MNRAS, 486, 3805
Binnie T., Pritchard J. R., 2019, MNRAS, 487, 1160
Bouwens R. J. et al., 2015, ApJ, 803, 34
Bouwens R. J. et al., 2016, ApJ, 830, 67
Bouwens R. J., Oesch P. A., Illingworth G. D., Ellis R. S., Stefanon M., 2017, ApJ, 843, 129
Bowman J. D., Rogers A. E., Monsalve R. A., Mozdzen T. J., Mahesh N., 2018, Nature, 555, 67
Bradley R. F., Tauscher K., Rapetti D., Burns J. O., 2019, ApJ, 874, 153
Bromm V., Larson R. B., 2004, ARA&A, 42, 79
Buchner J. et al., 2014, A&A, 564, A125
Ciardi B., Scannapieco E., Stoehr F., Ferrara A., Iliev I. T., Shapiro P. R., 2006, MNRAS, 366, 689
Clark S. J., Dutta B., Gao Y., Ma Y.-Z., Strigari L. E., 2018, Phys. Rev. D, 98, 043006
Dalla Vecchia C., Schaye J., 2008, MNRAS, 387, 1431
Dalla Vecchia C., Schaye J., 2012, MNRAS, 426, 140
Das A., Mesinger A., Pallottini A., Ferrara A., Wise J. H., 2017, MNRAS, 469, 1166
DeBoer D. R. et al., 2017, PASP, 129, 045001
Draine B. T., Bertoldi F., 1996, ApJ, 468, 269
Efstathiou G., 1992, MNRAS, 256, 43P
Evoli C., Mesinger A., Ferrara A., 2014, J. Cosmol. Astropart. Phys., 2014, 024
Ewall-Wice A., Chang T. C., Lazio J., Doré O., Seiffert M., Monsalve R. A., 2018, ApJ, 868, 63
Feroz F., Hobson M. P., 2008, MNRAS, 384, 449
Feroz F., Hobson M. P., Bridges M., 2009, MNRAS, 398, 1601
Feroz F., Hobson M. P., Cameron E., Pettitt A. N., 2019, Open J. Astrophys., 2, 10
Fialkov A., Barkana R., Visbal E., Tseliakhovich D., Hirata C. M., 2013, MNRAS, 432, 2909
Fialkov A., Barkana R., Cohen A., 2018, Phys. Rev. Lett., 121, 011101
Finkelstein S. L. et al., 2015, ApJ, 810, 71
Foreman-Mackey D., Hogg D. W., Lang D., Goodman J., 2013, PASP, 125, 306
Fragos T., Lehmer B. D., Naoz S., Zezas A., Basu-Zych A., 2013, ApJ, 776, L31
Furlanetto S. R., Oh S. P., Briggs F. H., 2006, Phys. Rep., 433, 181
Goodman J., Weare J., 2010, Commun. Appl. Math. Comput. Sci., 5, 65
Greig B., Mesinger A., 2015, MNRAS, 449, 4246
Greig B., Mesinger A., 2017, MNRAS, 472, 2651
Greig B., Mesinger A., 2018, MNRAS, 477, 3217
Greig B., Mesinger A., Koopmans L. V. E., 2020, MNRAS, 491, 1398
Haiman Z., Rees M. J., Loeb A., 1996, ApJ, 467, 522
Haiman Z., Rees M. J., Loeb A., 1997, ApJ, 476, 458
Haiman Z., Abel T., Rees M. J., 2000, ApJ, 534, 11
Hartwig T., Bromm V., Loeb A., 2018, MNRAS, 479, 2202
Heger A., Woosley S. E., 2010, ApJ, 724, 341
Hektor A., Hütsi G., Marzola L., Raidal M., Vaskonen V., Veermäe H., 2018, Phys. Rev. D, 98, 023503
Hill J. C., Baxter E. J., 2018, J. Cosmol. Astropart. Phys., 2018, 037
Hills R., Kulkarni G., Meerburg P. D., Puchwein E., 2018, Nature, 564, E32
Holzbauer L. N., Furlanetto S. R., 2012, MNRAS, 419, 718
Hopkins P. F., Kereš D., Oñorbe J., Faucher-Giguère C.-A., Quataert E., Murray N., Bullock J. S., 2014, MNRAS, 445, 581
Hopkins P. F. et al., 2018, MNRAS, 480, 800
Hui L., Gnedin N. Y., 1997, MNRAS, 292, 27
Jaacks J., Finkelstein S. L., Bromm V., 2018, MNRAS, 475, 3883
Jeffreys H., 1939, The Theory of Probability, Oxford Classic Texts in the Physical Sciences, 3rd edn. Oxford Univ. Press, Oxford
Johnson J. L., Greif T. H., Bromm V., 2007, ApJ, 665, 85
Keller B. W., Wadsley J., Benincasa S. M., Couchman H. M. P., 2014, MNRAS, 442, 3013
Kimm T., Katz H., Haehnelt M., Rosdahl J., Devriendt J., Slyz A., 2017, MNRAS, 466, 4826
Koh D., Wise J. H., 2018, MNRAS, 474, 3817
Kovetz E. D., Poulin V., Gluscevic V., Boddy K. K., Barkana R., Kamionkowski M., 2018, Phys. Rev. D, 98, 103529
Kulkarni M., Visbal E., Bryan G. L., 2020, preprint (arXiv:2010.04169)
Kunz M., Trotta R., Parkinson D. R., 2006, Phys. Rev. D, 74, 023503
Lai D. K., Bolte M., Johnson J. A., Lucatello S., Heger A., Woosley S. E., 2008, ApJ, 681, 1524
Liddle A. R., 2004, MNRAS, 351, L49
Liddle A. R., 2007, MNRAS, 377, L74
Liu B., Bromm V., 2020, MNRAS, 497, 2839
Livermore R. C., Finkelstein S. L., Lotz J. M., 2017, ApJ, 835, 113
Lopez-Honorez L., Mena O., Moliné Á., Palomares-Ruiz S., Vincent A. C., 2016, J. Cosmol. Astropart. Phys., 2016, 004
Ma X. et al., 2018, MNRAS, 478, 1694
McGreer I. D., Mesinger A., D'Odorico V., 2015, MNRAS, 447, 499
Machacek M. E., Bryan G. L., Abel T., 2001, ApJ, 548, 509
McKee C. F., Tan J. C., 2008, ApJ, 681, 771
McQuinn M., D'Aloisio A., 2018, J. Cosmol. Astropart. Phys., 2018, 016
McQuinn M., Zahn O., Zaldarriaga M., Hernquist L., Furlanetto S. R., 2006, ApJ, 653, 815
McQuinn M., Lidz A., Zahn O., Dutta S., Hernquist L., Zaldarriaga M., 2007, MNRAS, 377, 1043
Madau P., Dickinson M., 2014, ARA&A, 52, 415
Mebane R. H., Mirocha J., Furlanetto S. R., 2020, MNRAS, 493, 1217
Mena O., Palomares-Ruiz S., Villanueva-Domingo P., Witte S. J., 2019, Phys. Rev. D, 100, 043540
Mesinger A., ed., 2019, The Cosmic 21-cm Revolution, 2514-3433. IOP Publishing, Bristol, UK
Mesinger A., Furlanetto S., 2007, ApJ, 669, 663
Mesinger A., Johnson B. D., Haiman Z., 2006, ApJ, 637, 80
Mesinger A., Furlanetto S., Cen R., 2011, MNRAS, 411, 955
Mesinger A., McQuinn M., Spergel D. N., 2012, MNRAS, 422, 1403
Mesinger A., Greig B., Sobacchi E., 2016, MNRAS, 459, 2342
Mineo S., Gilfanov M., Sunyaev R., 2012, MNRAS, 419, 2095
Miralda-Escudé J., Haehnelt M., Rees M. J., 2000, ApJ, 530, 1
Miranda V., Lidz A., Heinrich C. H., Hu W., 2017, MNRAS, 467, 4050
Mirocha J., Furlanetto S. R., 2019, MNRAS, 483, 1980
Mirocha J., Mebane R. H., Furlanetto S. R., Singal K., Trinh D., 2018, MNRAS, 478, 5591
Mondal R., Bharadwaj S., Majumdar S., 2016, MNRAS, 456, 1936
Morales M. F., 2005, ApJ, 619, 678
Moster B. P., Naab T., White S. D. M., 2013, MNRAS, 428, 3121
Muñoz J. B., 2019, Phys. Rev. D, 100, 63538
Muñoz J. B., Loeb A., 2018, Nature, 557, 684
Mutch S. J., Geil P. M., Poole G. B., Angel P. W., Duffy A. R., Mesinger A., Wyithe J. S. B., 2016, MNRAS, 462, 250
Nagao T., Motohara K., Maiolino R., Marconi A., Taniguchi Y., Aoki K., Ajiki M., Shioya Y., 2005, ApJ, 631, L5
Nagao T. et al., 2008, ApJ, 680, 100
Nakatani R., Fialkov A., Yoshida N., 2020, preprint (arXiv:2007.08149)
O'Shea B. W., Wise J. H., Xu H., Norman M. L., 2015, ApJ, 807, L12
Oesch P. A., Bouwens R. J., Illingworth G. D., Labbé I., Stefanon M., 2018, ApJ, 855, 105
Pacucci F., Mesinger A., Mineo S., Ferrara A., 2014, MNRAS, 443, 678
Park J., Mesinger A., Greig B., Gillet N., 2019, MNRAS, 484, 933
Parsons A. R. et al., 2010, AJ, 139, 1468
Parsons A., Pober J., McQuinn M., Jacobs D., Aguirre J., 2012, ApJ, 753, 81
Patil A. H. et al., 2017, ApJ, 838, 65
Philip L. et al., 2019, J. Astron. Instrum., 8, 1950004
Planck Collaboration XLVII, 2016a, A&A, 596, A108
Planck Collaboration XIII, 2016b, A&A, 594, A13
Planck Collaboration VI, 2018, A&A, 641, A6
Pober J. C. et al., 2013, AJ, 145, 65

Pober J. C. et al., 2014, ApJ, 782, 66
Price D. C. et al., 2018, MNRAS, 478, 4193
Pritchard J. R., Furlanetto S. R., 2007, MNRAS, 376, 1680
Qin Y., Mesinger A., Park J., Greig B., Muñoz J. B., 2020, MNRAS, 495, 123
Rahmati A., Pawlik A. H., Raičević M., Schaye J., 2013, MNRAS, 430, 2427
Roederer I. U., Preston G. W., Thompson I. B., Shectman S. A., Sneden C., Burley G. S., Kelson D. D., 2014, AJ, 147, 136
Sanderbeck P. R. U., McQuinn M., D'Aloisio A., Werk J. K., 2018, ApJ, 869, 159
Santos M. G., Silva M. B., Pritchard J. R., Cen R., Cooray A., 2011, A&A, 527, A93
Schaerer D., 2002, A&A, 382, 28
Schauer A. T. P., Glover S. C. O., Klessen R. S., Ceverino D., 2019, MNRAS, 484, 3510
Schauer A. T. P., Drory N., Bromm V., 2020, ApJ, preprint (arXiv:2007.02946)
Shapiro P. R., Giroux M. L., Babul A., 1994, ApJ, 427, 25
Shaw A. K., Bharadwaj S., Mondal R., 2019, MNRAS, 487, 4951
Sims P. H., Pober J. C., 2019, MNRAS, 488, 2904
Singh S., Subrahmanyan R., Shankar N. U., Rao M. S., Girish B. S., Raghunathan A., Somashekar R., Srivani K. S., 2018, Exp. Astron., 45, 269
Skilling J., 2004, AIPC, 735, 395
Slatyer T. R., Wu C.-L., 2018, Phys. Rev. D, 98, 023013
Smidt J., Whalen D. J., Chatzopoulos E., Wiggins B., Chen K.-J., Kozyreva A., Even W., 2015, ApJ, 805, 44
Sobacchi E., Mesinger A., 2014, MNRAS, 440, 1662
Spinelli M., Bernardi G., Santos M. G., 2018, MNRAS, 479, 275
Suda T. et al., 2008, PASJ, 60, 1159
Sun G., Furlanetto S. R., 2016, MNRAS, 460, 417
Tacchella S., Bose S., Conroy C., Eisenstein D. J., Johnson B. D., 2018, ApJ, 868, 92
Thompson A. R., Moran J. M., , Swenson G. W., Jr, 2017, Interferometry and Synthesis in Radio Astronomy, 3rd edn. Springer, Berlin
Thoul A. A., Weinberg D. H., 1996, ApJ, 465, 608
Tingay S. J. et al., 2013, Publ. Astron. Soc. Aust., 30, e007
Tornatore L., Ferrara A., Schneider R., 2007, MNRAS, 382, 945
Trotta R., 2017, preprint (arXiv:1701.01467)
Tumlinson J., Shull J. M., 2000, ApJ, 528, L65
Turk M. J., Abel T., O'Shea B., 2009, Science, 325, 601
van Haarlem M. P. et al., 2013, A&A, 556, A2
Visbal E., Haiman Z., Bryan G. L., 2015, MNRAS, 453, 4456
Visbal E., Haiman Z., Bryan G. L., 2018, MNRAS, 475, 5246
Whalen D., van Veelen B., O'Shea B. W., Norman M. L., 2008, ApJ, 682, 49
Wise J. H., Abel T., 2007, ApJ, 671, 1559
Wise J. H., Turk M. J., Norman M. L., Abel T., 2012, ApJ, 745, 50
Wolcott-Green J., Haiman Z., Bryan G. L., 2011, MNRAS, 418, 838
Wyithe J. S. B., Loeb A., 2013, MNRAS, 428, 2741
Xu H., Ahn K., Norman M. L., Wise J. H., O'Shea B. W., 2016a, ApJ, 832, L5
Xu H., Wise J. H., Norman M. L., Ahn K., O'Shea B. W., 2016b, ApJ, 833, 84
Yoshida N., Sokasian A., Hernquist L., Springel V., 2003, ApJ, 598, 73
Yoshida N., Omukai K., Hernquist L., Abel T., 2006, ApJ, 652, 6
Yung L. Y. A., Somerville R. S., Popping G., Finkelstein S. L., Ferguson H. C., Davé R., 2019, MNRAS, 490, 2855
Zahn O., Mesinger A., McQuinn M., Trac H., Cen R., Hernquist L. E., 2011, MNRAS, 414, 727

This paper has been typeset from a TEX/LATEX file prepared by the author.